Plasmon-assisted directional infrared photoluminescence of HgTe nanocrystals

Erwan Bossavit, Tung Huu Dang, Puyuan He, Mariarosa Cavallo, Adrien Khalili, Corentin Dabard, Huichen Zhang, Djamal Gacemi, Mathieu Silly, Claire Abadie, et al.

Plasmon-assisted directional infrared photoluminescence of HgTe nanocrystals

Erwan Bossavit[1,2], Tung Huu Dang[1,3], Puyuan He[4], Mariarosa Cavallo[1], Adrien Khalili[1], Corentin Dabard[1], Huichen Zhang[1], Djamal Gacemi[3], Mathieu G. Silly[2], Claire Abadie[1], Bruno Gallas[1], Debora Pierucci[1], Yanko Todorov[3], Carlo Sirtori[3], Benjamin T. Diroll[5], Aloyse Degiron[4], Emmanuel Lhuillier[1*], Angela Vasanelli[3*]

[1] Sorbonne Université, CNRS, Institut des NanoSciences de Paris, INSP, F-75005 Paris, France.
[2] Synchrotron SOLEIL, L'Orme des Merisiers, Départementale 128, 91190 Saint-Aubin, France.
[3] Laboratoire de Physique de l'Ecole Normale Supérieure, ENS, Université PSL, CNRS, Sorbonne Université, Université Paris Cité, 75005 Paris, France
[4] Université Paris Cité, CNRS, Laboratoire Matériaux et Phénomènes Quantiques, 75013 Paris, France.
[5]Center for Nanoscale Materials, Argonne National Laboratory, 9700 S. Cass Avenue, Lemont, Illinois 60439, United States

Abstract: HgTe nanocrystals offer a unique spectral tunability with both absorption and emission covering the near and mid-infrared as well as the THz window. Nevertheless, a very limited amount of work has been dedicated to electroluminescence from this material. An efficient diode not only requires designing a structure that achieves a high electrical efficiency (i.e., efficient electron and hole injections), but also finding a way to efficiently extract the emitted photons. The shift from visible to infrared certainly demands revisiting the strategies proposed for shorter wavelengths (microlens arrays). Here we demonstrate that a metallic grating can be used to enhance the PL signal up to a factor 4 while enabling directionality in the emission, which is driven by the grating period.

*To whom correspondence should be sent: angela.vasanelli@ens.fr, el@insp.upmc.fr

1. INTRODUCTION

The bright and continuously tunable luminescence exhibited by nanocrystals has driven the interest in using these nanoparticles as active materials for optoelectronic applications. Whereas CdSe and InP dominate applications in the visible range, narrower band gap semiconductors are required to cover the infrared spectral range. HgTe[1], a semimetal in bulk, behaves as a semiconductor in the presence of quantum confinement[2]. Its lack of bulk band gap enables a unique tunability: from the visible for the strongly confined form of HgTe (*i.e.,* the 2D nanoplatelets[3,4]) to the THz range[5] for the largest particles with size above the Bohr radius (40 nm in HgTe[6]). Furthermore, this spectral tunability is no longer limited to absorption, and luminescence can be obtained from 0.8 to 5 µm[7–11] and, more recently, has also been demonstrated in the THz range[12].

An effort has also been dedicated to electroluminescence based on HgTe NCs. Initial works have been focused on the near-infrared[13–16]/telecom range where core-only NCs present a high photoluminescence efficiency: values above 30 % have been reported by several groups[17,18]. However, up to telecom wavelengths, NCs suffer from competition with existing technologies, in particular with epitaxially grown III-V quantum wells. This makes recent demonstrations of electroluminescence above 2 µm from HgTe NCs[19,20] far more interesting since the range from 1.5 to 4 µm corresponds to a technological gap where bright sources remain challenging to design. The integration of HgTe NCs into light emitting diodes (LEDs) faces two main problems: (i) a reduced PL efficiency when the NCs are switched from solution to film form, and (ii) an overall inefficient light extraction. Though films of NCs present a reduced refractive index (≈2) compared to III-V semiconductors (n>3), most of the emitted photons in HgTe NC-based LEDs still end up waveguided along the substrate and generate thermal losses rather than useful light. This is a common problem related to randomly-oriented emission which limits the efficiency of all LEDs to approximately 20 %. However, controlling emission orientation, which is advanced in organic LEDs[21], improves the fraction of light escaping the device and lifts the 20 % external quantum efficiency ceiling. It thus appears of utmost interest to develop strategies that can boost the PL signal at the film scale while enabling directional emission to extract the generated photons from the diode stack in an efficient way. One strategy is to macroscopically align inherently anisotropic emitters. A different and more general strategy will be to couple the NC film to a photonic cavity. In the context of infrared sensing, this approach has generated a significant amount of work to enhance[22–27] device absorption, reshape the spectral response[28,29] or enable a bias reconfigurable response[30,31]. However, far less work has been focused on using photonic structures[32,33] to enhance outcoupled PL signal of infrared-emitting NC films[34–38], and even less for HgTe films in particular[39,40]. Sergeev *et al.* have proposed coupling HgTe NC emitters to a laser-printed bump array[39] and achieved a five-fold enhancement of the PL. Though spectacular, the transfer of the bump array within a diode stack will not be a straightforward process since the bump size is larger than the conventional thickness of a diode. Here, we explore how a simple, compact plasmonic grating can enhance the PL signal and provide directionality to the emission of an inherently isotropic emitter.

2. RESULTS AND DISCUSSION

2.1. Infrared luminescent properties of HgTe nanocrystals

As a model system, we start with HgTe NCs with a band gap at around 1.3 µm. Though less promising than longer wavelength materials, operation at this wavelength is more easily compatible with existing optical setups, thus enabling both time- and wavevector-resolved measurements. The particles are grown using the procedure developed by Geiregat *et al*[41], during which mercury chloride is reacted with trioctylphosphine telluride in a medium containing oleylamine as the coordinating solvent and dodecanethiol as stabilizing ligands. The reaction is performed at a low temperature (60°C) to limit particle growth. This leads to particles with sizes in the 5-6 nm range

according to transmission electron microscopy, see **Figure 1**b. The associated absorption spectrum (**Figure 1**a) depicts a sharp edge with a maximum at 1100 nm. The particles present a Stoke-shifted photoluminescence signal that presents a maximum at 1250 nm.

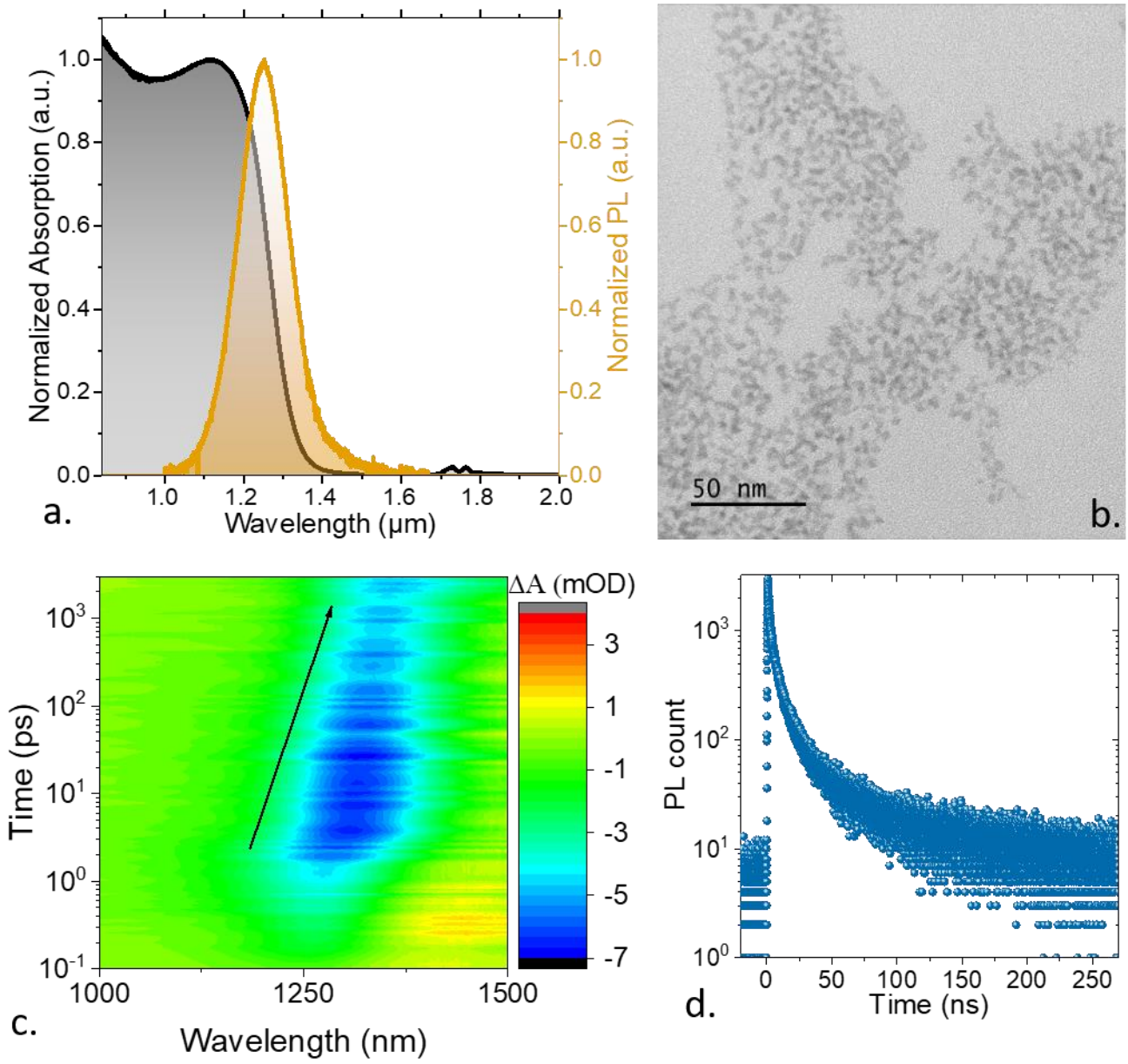

Figure 1 HgTe NCs as infrared emitters*. a. Absorption and photoluminescence spectra for HgTe NCs. b. TEM image of the HgTe NCs. c. Two-dimensional transient absorption map as a function of wavelength and time for HgTe NCs in solution. Excitation is done at 700 nm with a fluence of 15 µJ.cm^{-2}. d. Time-resolved PL for HgTe NCs under film form deposited on Si wafer. Excitation is done with 640 nm picosecond pulses with a repetition rate of 1 MHz.*

Transient absorption spectroscopy reveals a spectral redshift of the band edge feature over time, see **Figure 1**c. This effect can be connected to the fact that, in such small nanocrystals, trap states are formed in the vicinity of the valence band and create with the latter a three-level system enabling low threshold stimulated emission[41]. This effect can also be connected to the spectral redshift occurring over time observed in HgTe 2D nanoplatelets[42,43], which may be interpreted as a shift over time from a band edge emission to a trap-driven emission process. Further evidence that traps are involved in emission is observed in the time-resolved PL (TRPL) signal, see **Figure 1**d, which presents a multiexponential character. Moreover, we observe a clear delay of the PL signal as the emitted wavelength is redshifted, see Figure S1, a process consistent with a slow relaxation from band edge state toward trap emitting states. Finally, previous studies have pointed out that the

exciton emission has a characteristic radiative decay time of a few nanoseconds, whereas the tail of emission occurring at long time scales is related to trap emission[13].

To cure the formed traps, the films are treated with HgI_2 dissolved in methanol as proposed before by Bossavit *et al.*[14]. In the initial procedure, a two-step ligand exchange is performed in which a short thiol (mercaptopropionic acid = MPA) is first used to harden the film to enable later deposition of additional layer. However, this step also induces a significant quenching of the PL signal. In a diode stack, this step is important to deposit subsequent layers without damaging the HgTe NC film. In our case, we favor a process that maintains a high PL signal (*i.e.,* without MPA) since we do not aim to build a full diode in this work. We nevertheless checked that the main conclusion remains the same for the film after ligand exchange, see Figure S9-11. Actually, the quenching of the PL resulting from the use of MPA improves the contrast between the uncoupled PL and the PL coupled to the photonic structure.

2.2. Plasmon assisted Infrared luminescence

To gain control of the PL signal, we then couple it to a metallic grating[44–48], as schematized in **Figure 2**a. In such a metallic grating, a surface plasmon can be generated under transverse magnetic (TM) polarization with a resonance wavelength (λ_0) driven by the grating period (p) through: $p = \lambda_0/n_{eff}$, with n_{eff} the effective index of the surface plasmon mode, see Supplementary information. This effective index is expected to be smaller than the refractive index of the active material, due to the fact that the surface plasmon is also leaking into the air region. We have measured the optical index of the HgTe film using spectrally resolved ellipsometry and found n=2, see Figure S2. Note that this value is lower than the value of 2.3 typically obtained for HgTe NC films used for photodetection[49]. We can relate this reduced refractive index to the milder conditions of the film preparation. Indeed, this preparation does not systematically remove the initial long capping ligands from the NCs that are used in order to maintain PL at the cost of lower electronic coupling. To achieve a resonance around 1250 nm, we designed a series of grating with periods ranging from 600 to 900 nm, while the gold strip width is kept constant at 300 nm. Such gratings are fabricated using e-beam lithography. It is worth noting that if a similar concept should be extended toward longer emission wavelengths, the resonant period will be larger and thus conventional optical lithography may be used to design the grating for mid IR nanocrystals.

A scanning electron microscopy image of a grating is shown in **Figure 2**b. Electromagnetic simulation shows that surface plasmons are formed at the interface between the gold strip and HgTe film under TM polarization, see **Figure 2**c. For a 200 nm NC film, the surface plasmon electric field overlaps well with the NCs in the vicinity of the gold stripes. The spectral position of this surface plasmon resonance is set by the grating period.

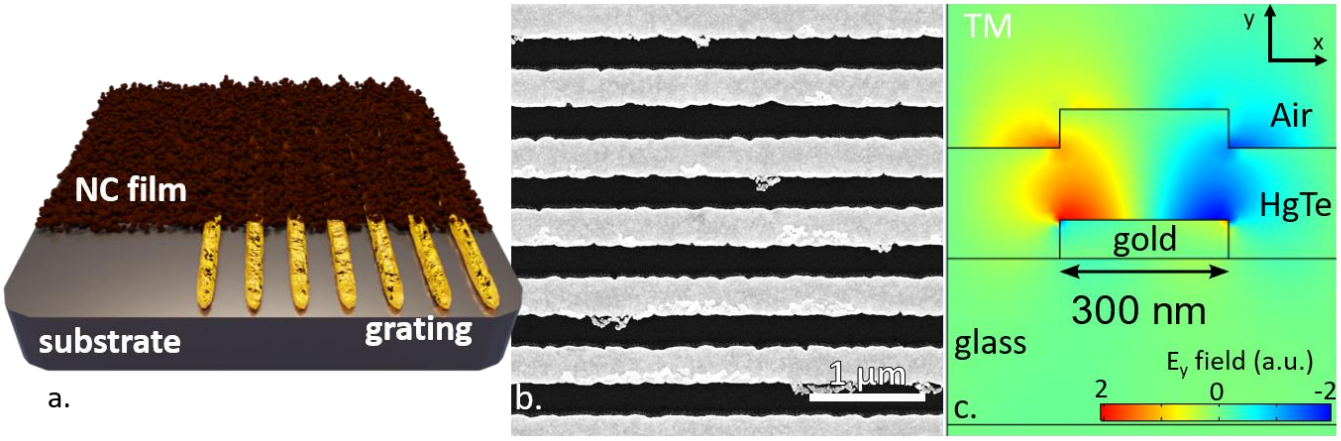

Figure 2 HgTe NC film coupled to a grating. *a. Schematic representation of the grating-functionalized subtrate, coated with a NC film. b. Scanning electron microscopy image of the gold grating. c. Electric field map in TM polarization.*

A photonic structure can affect an emitter in three distinct manners: (*i*) it can enhance its absorption through an enhancement of the local electric field, (*ii*) the Purcell effect can tune the ratio between radiative and non-radiative decay paths, and finally (*iii*) an antenna effect can shape the radiative pattern.

As we couple a thin (50 nm) film of HgTe NCs to the gratings, we observe a dramatic quenching of the PL signal, see **Figure 3**a and d and S3. This behavior is expected according to standard textbook theory because non-radiative transfers dominate the interactions when emitters are placed at vanishing distance to metals, ultimately resulting in Joule losses in such optically lossy materials[48,50]. This result contrasts with what has been observed for other quantum dots, such as PbS[36,37] and CdSe/CdS[51] , for which an enhancement of the PL for thin films has been observed in similar systems (NCs coupled with metallic resonators, metallic mirrors). In these cases, a Kirchhoff law[52] point of view has been used, in which the NCs do not act as individual emitters but rather as an effective medium. additional PL measurements reveal a significant redshift of the spectrum when the pump power increases (Figure S4), indicating a significant contribution of trap states to the PL signal as pointed out in the first part of the paper in **Figure 1**d and S1. The trap states of neighboring NCs are probably even less prone to interact mutually than excitons. We thus expect that our NCs operate in a weak tunnel coupling regime, which results in a behavior of individual emitters.

Two strategies have been explored to overcome this quenching: introducing a dielectric spacer (**Figure 3**b and e) and using a thicker HgTe film of 200 nm. In the latter case, the bottom part of the film effectively acts as the spacer (**Figure 3**c and f). In both cases, the PL signal over the grating appears enhanced (+60 % over the 600 nm period grating, see **Figure 3**g and h). Whereas the magnitude of the signal is increased, it appears only marginally shifted or broadened, see **Figure 3**h. It is worth mentioning that in the case of the ligand-exchanged film (Figure S10) the improvement appears even stronger due to the stronger quenching of the PL not coupled to the grating.

Furthermore, microscopy-coupled TRPL reveals that the emission dynamics are the same on the bare substrate and the grating area, see Figure S6. We can thus rule out a Purcell effect as a possible mechanism to explain the PL magnification. PL enhancement is also observed as 200 nm HgTe film is deposited on a continuous gold film (Figure S3). We can correlate the enhancement of the PL to two effects. On the one hand, there is an expected enhancement of the absorption at the

excitation wavelength (633 nm here), see Figure S8. On the other hand, for the bare silica substrate, the PL signal is mainly guided toward the substrate due to the higher optical index of silica compared to air, which is not the case on a gold substrate. In the presence of gold, both the absorption and the emission are thus enhanced proportionally to the filling factor of gold in the grating.

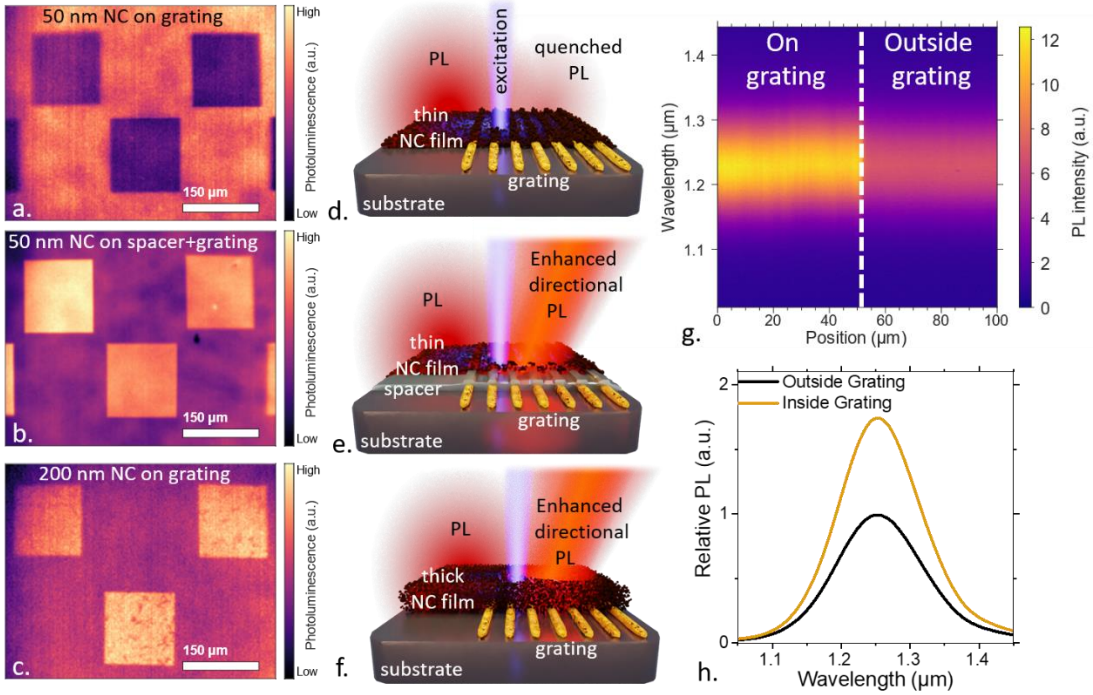

Figure 3 Photoluminescence on grating. *a. Image of the PL from HgTe NCs over the area corresponding to three gratings (dark squares) for a thin (50 nm) NC film directly deposited on the substrate. b. Image of the PL from HgTe NCs over the area corresponding to three gratings (light squares) for a thin (50 nm) NC film deposited over a thin dielectric spacer (40 nm Al_2O_3) on top of the grating-functionalized substrate. c. Image of the PL from HgTe NCs over the area corresponding to three gratings (light squares) for a thick (200 nm) NC film directly deposited on the substrate. Parts d to e are schematic representations of the experiments described respectively in a, b and c. g. PL spectra across an area corresponding to the interface between a grating (p=600 nm) and the bare substrate. h. PL spectra over and outside of the 600 nm gold grating. Parts g and h are acquired in the case of thick HgTe NC film.*

Because the PL enhancement appears proportional to the gold coverage in the grating[53], we then update our geometry and build the gold grating on a gold substrate. By doing so, the PL enhancement now reaches 100 % (with respect to gold), see **Figure 4**f, corresponding to a total factor of 4 with respect to the NC deposited on the bare Si/SiO_2 substrate, see Figure S3. To summarize, the PL enhancement is a combination of several effects: (i) an increased absorption at the excitation wavelength due to the reflection of the incident beam on gold and the consequent multiple pass through the QD film; (ii) the gold mirror preventing the guiding of the emitted light toward the substrate and (iii) the coupling to the surface plasmon, which increases the electric field at the emission wavelength of the QDs, thus increasing the emission.

In addition, the surface plasmon also induces a preferential orientation of the PL signal. This last aspect is shown in the dispersion maps, see **Figure 4**a-c. Dispersion maps of the PL intensity versus wavevector are obtained by imaging the back focal plane of the microscope objective to measure the angular distribution of emission, with $k/k_0=0$ being normal to the surface. This is further enhanced with spectral resolution using a monochromator. Whereas the PL signal on a continuous gold film

reveals a non-dispersive emission (Figure S3d), additional features appear for the PL emission from grating areas. The latter is now composed of a continuous non-dispersive background, over which tilted lines corresponding to the surface plasmon dispersion can be well identified, see Figure S7. The period of the grating sets the energy where those lines cross, as presented in **Figure 4**a-c. The effective index of the surface plasmon mode can be extracted from $n_{eff} = \lambda_{crossing}/p$. We found n_{eff} values of 1.55, 1.53, and 1.5 for p values of 600 nm, 700 nm, and 800 nm, respectively, see Figure S6. Practically, the grating structure allows controlling the direction of the PL emission. For a 700 nm period, the grating enhances the PL signal at large wavevectors. Thus, the emission preferentially occurs at a titled angle, as shown in **Figure 4**d. Conversely, with a 900 nm period grating, the diffraction maximizes the signal at normal incidence (**Figure 4**e). This situation is typically the one of interest for LEDs where emission needs to occur at normal incidence to avoid waveguiding. In the case of ligand-exchanged films, the spectral changes can be even more dramatic as the weight of the isotropic emission is reduced with respect to the emission coupled to the dispersive plasmon. As a result, new peaks can be observed for the PL spectrum depending on the actual direction of emission, see Figure S11. Note that the same concepts can be used for emission enhancement and directionality of a LED. However, in this case the 1D grating will have to be replaced by a 2D grid to maximize the light extraction.

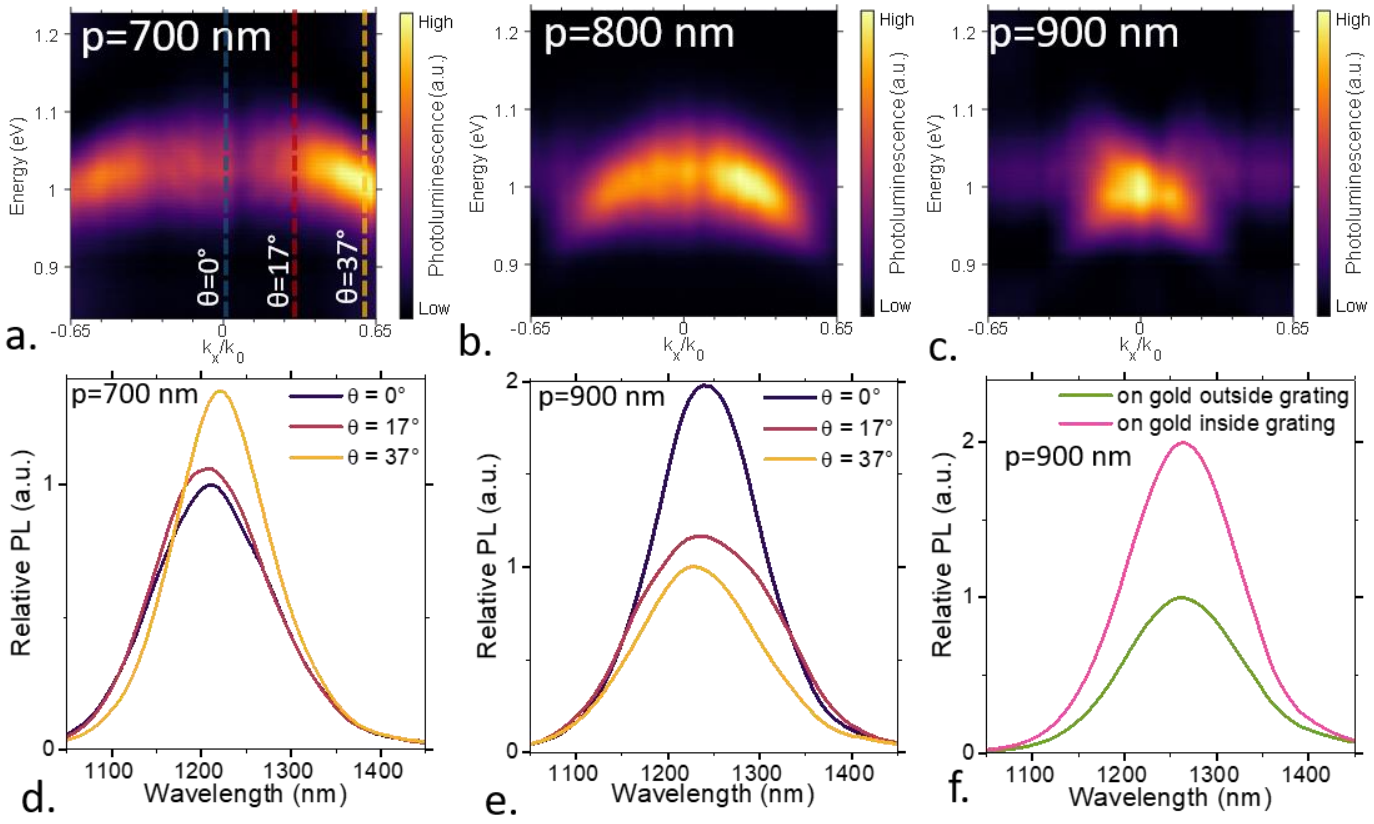

Figure 4 Dispersion maps. 2D dispersion map of the PL *as a function of energy and wavevector for a grating of 700 nm (a.), 800 nm (b.) and 900 nm (c.). d. . (resp e.) PL spectra along three different directions for the 700 nm (resp 900 nm) period grating. f. Relative PL signal on gold and for a grating (p=900 nm) on gold. Data are acquired in the case of thick (200 nm) HgTe NC film.*

3. CONCLUSION

We demonstrate a simple strategy to achieve directional emission from a HgTe NC film with operation in the near-infrared. Coupling the PL signal to the diffraction mode of a metallic grating

enables a PL enhancement by 400 % with respect to the same material deposited on bare substrate, while directional emission can be favored perpendicular to the substrate through a careful choice of the grating period. The next challenge will be to transfer this concept to a full diode stack in which the complete dielectric environment needs to be considered. For this application, the metallic grating can also provide one of the electrical contacts of the diode stack. The transfer is nevertheless not trivial since the whole dielectric environment is changed compared to the current situation, asking for deep updates in simulation models as well as determining the complex index of all involved layers. Another difficulty may result from planar transport occurring if the opening in the metallic grating becomes larger than the diode stack thickness. This will likely lead to excess voltage being required, which may increase the bias threshold for the diode.

4. Experimental section

Chemicals: Mercury chloride ($HgCl_2$, Sigma Aldrich, 99%), Mercury iodide (HgI_2, Touzart & Matignon), Tellurium powder (Te, Alfa Aesar, 99.99%), trioctylphosphine (TOP, thermofisher scientific, 90%), Oleylamine (OLA, Acros, 80-90%), Dodecanethiol (DDT, Sigma-Aldrich, 98%), Methanol (Carlo Erba, 99.8%), Toluene (Carlo Erba, 99.3%), acetone (VWR), isopropanol (IPA, VWR), methylisobutylketone (MIBK, VWR, >98.5%). All chemicals are used as received, except oleylamine which is centrifuged before used. **Mercury compounds are highly toxic. Handle them with special care.**

1 M TOP:Te precursor: 6.35 g of Te powder was mixed in 50 mL of TOP in a three-neck flask. The flask was kept under vacuum at room temperature for 5 min and then the temperature was raised to 100 °C. Furthermore, degassing of flask was conducted for the next 20 min. The atmosphere was switched to Ar and the temperature was raised to 275 °C. The solution was stirred until a clear orange coloration was obtained. The flask was cooled down to room temperature and the color switched to yellow. Finally, this solution was transferred to a nitrogen-filled glove box for storage.

HgTe nanocrystal synthesis : The synthesis is taken from Geiregat *et al.*[41] In a 100 mL three-neck flask, 810 mg of $HgCl_2$ (3 mmol), 4.8 mL (18 mmol) of dodecanethiol and 24 mL of oleylamine are degassed under vacuum at 110 °C for 30 min. The atmosphere is switched to N_2 and the temperature is set to 60 °C. When the temperature stabilizes at 60 °C, 3 mL of TOP:Te solution (1 M) are quickly injected, and the growth is allowed for 1 min. The reaction is quenched by injecting 20 mL of toluene. A water bath is used to further cool down the mixture. Another 10 mL of toluene are finally added to further dilute the solution. The reaction mixture is evenly distributed in 3 centrifuge tubes, then precipitated with 15 mL of methanol for each tube, and centrifuged. The supernatant is discarded and the nanocrystals in each tube are redispersed in 5 mL of toluene, with a single drop of DDT added. Then a centrifugation is conducted while the mixture is in toluene to remove the colloidally unstable parts. The three tubes are merged into one. The process of precipitation/redispersion with methanol and toluene is carried out a second time. The solution is then precipitated a final time and left to dry under vacuum for 30 min. The nanocrystals are dispersed in a minimum amount of toluene, so that their optical density at 400 nm is measured to be 0.5 after a 5000 times dilution. This corresponds to an estimated 170 g/L mass concentration. The solution is stored in a freezer at -20°C and filtered with a 0.22 µm PTFE filter before use.

Transmission electron microscopy: A drop of a diluted nanocrystals solution was drop-casted on a copper grid covered with an amorphous carbon film. The grid was degassed overnight under secondary vacuum. Imaging was conducted using a JEOL 2010 transmission electron microscope operated at 200 kV.

Infrared spectroscopy is conducted using a Fisher IS50 Fourier transform Infrared spectrometer. To measure NCs absorption, we use the spectrometer in ATR configuration. A drop of NC solution is dried onto the diamond cell. The source is a white light, the beam splitter is made of CaF_2 and the detector is a DTGS ATR. Spectra are typically acquired between 12 000 cm^{-1} and 2000 cm^{-1} with a 4 cm^{-1} resolution while averaging over 32 spectra. For PL measurement, a drop of NC solution is dried on a glass slide and illuminated by a blue flashlight. This signal is then fed into the same FTIR and used as source. The same CaF_2 beamsplitter is used. For detection, we use an InGaAs detector with sensitivity expanded up to 2.5 µm.

Time-resolved photoluminescence: The decay traces were obtained with a time-correlated single photon counting (TCSPC) setup. An inverted Olympus IX73 microscope equipped with a 50X objective was used to focus the picosecond pulses of a PicoQuant laser diode onto the sample. The central wavelength of the pulses was 640 nm and the repetition rate 1 MHz. The near-infrared photoluminescence signal was collected with the same objective, then separated from the pump using a dichroic mirror (DMLP950R from Thorlabs) and finally directed with a multimode optical fiber toward an InGaAs single photon detector ID230 from ID Quantique. The TCSPC histograms were built with a PicoHarp 300 module from PicoQuant, using the trigger signal from the laser diode driver and the data sent by the ID230 detector.

Transient absorption: Transient absorption measurements were performed by splitting the 800 nm fundamental of a 5 kHz, 60 fs Ti: sapphire laser into pump and probe branches. The pump branch was directed through an OPA to generate 700 nm pump pulses and chopped to 2.5 kHz; the probe branch was optically delayed using a variable delay stage with retroreflector and then focused into a 5 mm thick sapphire plate to generate a supercontinuum in the near-infrared. The pump and probe pulses were spatially-overlapped at the sample position and spectra were collected by differencing pump-on and pump-off spectra.

Optical ellipsometry: The spectroscopic ellipsometry measures the changes in the polarization state between the incident and the reflected light characterized by the angles ψ and Δ.

$$\rho = \frac{r_p}{r_s} = \left|\frac{r_p}{r_s}\right| e^{i(\delta_p - \delta_s)} = \tan\psi\, e^{i\Delta}$$

where r_p and r_s are the reflection coefficients of p and s polarized light respectively and where δ_p.and δ_s are the phase shifts at reflection in p and s polarizations, respectively. The measurements were performed on a V-VASE ellipsometer (J.A. Woollam) in the 350-2500 nm range in steps of 10 nm and at the angles of incidence of 55° and 65°. The optical constants of the films were described as a superposition of Tauc-Lorentz and Gauss oscillators[49] and inserted in an effective medium approximation to account for the air and ligands in the films.

Input for electromagnetic simulation: For the air and Si substrate, the real parts of the refractive indices are set to 1 and 3.5, respectively, and the imaginary parts are both set to 0. For the natural

SiO_2 layer, refractive index is set to 1.5. For gold, the dielectric function from Drude model ε(E) = 1 – 2.29 x 10^7/ [E(E+i130)], with E the photon energy in meV, is used. For the NC film, the real and imaginary part of the refractive index measured with ellipsometry are used, as shown in Figure S2.

Here, the NC surface chemistry is treated quite differently from the film dedicated to transport. In particular, the ligand exchange avoids the use of short thiol that tends to quench the PL signal. This comes at the cost of a less dense film. As a consequence of this lower filling factor, the refractive index (≈2 instead of 2.3) and extinction coefficient at the band edge (≈0.05 instead of 0.1) are clearly reduced compared to the value obtained for film dedicated to transport[49].

Simulations: Optical properties of the structure are simulated with COMSOL Multiphysics, *2D Frequency Domain Interface*. Periodicity is set for boundary conditions at the side edges. A periodic port to generate incoming electromagnetic wave is placed above the structure (*i.e.,* in the region defined as air). Above the air and below the Si substrate, two perfectly matched layers are added to absorb outgoing waves and minimize possible nonphysical reflections due to limited size. Physical-controlled mesh is enabled with extremely fine element size. The dissipated power per unit volume in the metals and nanocrystals can be calculated using the formula $P = -0.5\omega|F|^2 Im(\varepsilon)$, where F is the electric field, ω is the angular frequency of the incident wave, and $Im(\varepsilon)$ is the imaginary part of the material permittivity. The absorption of one material is calculated by integrating the dissipated power over the volume of the material, then divided by the incident power defined in the port.

Grating fabrication: In a cleanroom, Si/SiO_2 substrates (400 nm oxide layer) are thoroughly washed by first spraying them with acetone then sonicating them in an acetone bath for 5 min. Acetone is sprayed a second time followed by IPA, which is dried with N_2. The substrates are then put into an O_2 plasma cleaner for 7 minutes at 30 W. Once the substrates are cleaned PMMA is deposited on top to prepare them for E-beam lithography. Roughly 300 nm of PMMA are deposited by spin-coating a pre-prepared solution of PMMA in anisole at 4000 rpm for 30 seconds, followed by 3 minutes of annealing at 175°C on a heating plate. Thus prepared, the substrates are put into a Zeiss Supra 40 SEM with Raith ELPHYS Quantum device and e-beam lithography is performed according to the grating design. The operating bias is set to 20 kV, the aperture to 10 µm, and the dose to 160 µC/cm². The PMMA is then developed in an MIBK:IPA solution (1:3) for 60s, then washed with IPA and dried with N_2. The developed substrates are cleaned in an O_2 plasma cleaner for 3 minutes at 30 W. Using a VINCI thermal evaporator, 5 nm of Ti followed by 50 nm of Au are deposited. The PMMA is lifted-off by putting the substrates in acetone for 1 day. Once cleaned a last time for 3 minutes in an O_2 plasma cleaner at 30 W, the substrates are ready for film deposition.

Alumina layer deposition: When needed, an alumina spacer is introduced between the gold grating and the NC film. An Anric AT-400 Atomic Layer Deposition (ALD) system is employed to deposit 40 nm of Al_2O_3. 450 cycles of ALD are performed, each with pulsed trimethylaluminium (TMA) and H_2O reacted at 175 ºC. The Al_2O_3 film thickness is measured with reflectometry after the deposition.

Thin film deposition: HgTe NCs are deposited into thin films on top of the grating using spin coating. Before deposition, the solution is first diluted as desired then centrifuged for 2 min, filtered with a 0.22 µm PTFE filter, and sonicated for 1 min. Two different thicknesses are deposited. 200 nm, or 50 nm, of NCs are deposited by spin coating the HgTe solution at the initial concentration, or respectively at a fourth of the initial concentration, for 60 seconds at 2000 rpm. The films are then treated with HgI_2, in order to passivate the NCs' surface[14] and enhance the PL signal for the

characterization of the grating. An optimal enhancement is reached by dipping the films as deposited into a 5 mM HgI_2 solution in methanol, for 60 s or 15 s, for the 200 nm and 50 nm thicknesses respectively. The films are then washed by dipping them in methanol, and dried with N_2. After this final step, the films are ready to be characterized and are stored in a N_2-filled glovebox.

Photoluminescence characterization of the grating: The photoluminescence is measured using an Olympus BX51WI upright microscope with wide field Köhler illumination for the optical pumping (light source: a tungsten incandescent bulb filtered with a Thorlabs FESH0800 short pass filter and a Thorlabs DMLP950R dichroic mirror to remove the UV and infrared part of the spectrum). The 50X near-infrared objective used for optical pumping also serves to collect the photoluminescence. The latter is separated from the optical pump with the dichroic mirror and imaged onto an InGaAs camera (Princeton Instruments NIRvana 640ST) with the help of a 20 mm Telan lens (an additional longpass colored glass filter is put in front of the camera to remove any remnant of visible light). To obtain a dispersion map (*i.e.* mapping in the k space), a Bertrand lens is inserted in the optical path after the dichroic mirror to image the back focal plane of the microscope objective. A monochromator (Princeton Instruments Acton SP2356) mounted before the InGaAs camera provides the spectral information.

SUPPORTING INFORMATION

Supporting Information include details about (*i*) nanocrystals growth, (*ii*) procedure for material characterization, (*iii*) design fabrication and characterization of the metallic grating, (*iv*) discussion on the origin of quenching on gold

ACKNOWLEDEGMENTS

The project is supported by ERC grants blackQD (grant n° 756225), FORWARD (grant n° 771688) and AQDtive (grant n°101086358). We acknowledge the use of clean-room facilities from the “Centrale de Proximité Paris-Centre”. This work was supported by French state funds managed by the Agence Nationale de la Recherche through the grant Copin (ANR-19-CE24-0022), Frontal (ANR-19-CE09-0017), Graskop (ANR-19-CE09-0026), NITQuantum (ANR-20-ASTR-0008), Bright (ANR-21-CE24-0012), MixDFerro (ANR-21-CE09-0029) and Quicktera (ANR-22-CE09-0018). This project has received financial support from the CNRS through the MITI interdisciplinary programs.

CONFLICT OF INTEREST

The authors declare no competing financial interest.

KEYWORDS : nanocrystals, infrared, plasmon, photoluminescence, HgTe.

Data availability

The data that support the findings of this study are available from the corresponding author upon reasonable request.

REFERENCES

[1] C. Gréboval, A. Chu, N. Goubet, C. Livache, S. Ithurria, E. Lhuillier, *Chem. Rev.* **2021**, *121*, 3627.
[2] M. Green, H. Mirzai, *J. Mater. Chem. C* **2018**, *6*, 5097.
[3] B. T. Diroll, B. Guzelturk, H. Po, C. Dabard, N. Fu, L. Makke, E. Lhuillier, S. Ithurria, *Chem. Rev.* **2023**.

[4] E. Izquierdo, A. Robin, S. Keuleyan, N. Lequeux, E. Lhuillier, S. Ithurria, *J. Am. Chem. Soc.* **2016**, *138*, 10496.
[5] N. Goubet, A. Jagtap, C. Livache, B. Martinez, H. Portalès, X. Z. Xu, R. P. S. M. Lobo, B. Dubertret, E. Lhuillier, *J. Am. Chem. Soc.* **2018**, *140*, 5033.
[6] V. Rinnerbauer, K. Hingerl, M. Kovalenko, W. Heiss, *Appl. Phys. Lett.* **2006**, *89*, 193114.
[7] A. Rogach, S. V. Kershaw, M. Burt, M. T. Harrison, A. Kornowski, A. Eychmüller, H. Weller, *Adv. Mater.* **1999**, *11*, 552.
[8] S. Keuleyan, E. Lhuillier, P. Guyot-Sionnest, *J. Am. Chem. Soc.* **2011**, *133*, 16422.
[9] S. Keuleyan, J. Kohler, P. Guyot-Sionnest, *J. Phys. Chem. C* **2014**, *118*, 2749.
[10] K. A. Sergeeva, K. Fan, A. A. Sergeev, S. Hu, H. Liu, C. C. Chan, S. V. Kershaw, K. S. Wong, A. L. Rogach, *J. Phys. Chem. C* **2022**, *126*, 19229.
[11] M. V. Kovalenko, E. Kaufmann, D. Pachinger, J. Roither, M. Huber, J. Stangl, G. Hesser, F. Schäffler, W. Heiss, *J. Am. Chem. Soc.* **2006**, *128*, 3516.
[12] T. Apretna, N. Nilforoushan, J. Tignon, S. Dhillon, F. Carosella, R. Ferreira, E. Lhuillier, J. Mangeney, *Appl. Phys. Lett.* **2022**, *121*, 251101.
[13] J. Qu, P. Rastogi, C. Gréboval, D. Lagarde, A. Chu, C. Dabard, A. Khalili, H. Cruguel, C. Robert, X. Z. Xu, S. Ithurria, M. G. Silly, S. Ferré, X. Marie, E. Lhuillier, *Nano Lett.* **2020**, *20*, 6185.
[14] E. Bossavit, J. Qu, C. Abadie, C. Dabard, T. Dang, E. Izquierdo, A. Khalili, C. Gréboval, A. Chu, S. Pierini, M. Cavallo, Y. Prado, V. Parahyba, X. Z. Xu, A. Decamps-Mandine, M. Silly, S. Ithurria, E. Lhuillier, *Adv. Opt. Mater.* **2022**, *10*, 2101755.
[15] D. S. Koktysh, N. Gaponik, M. Reufer, J. Crewett, U. Scherf, A. Eychmüller, J. M. Lupton, A. L. Rogach, J. Feldmann, *ChemPhysChem* **2004**, *5*, 1435.
[16] É. O'Connor, A. O'Riordan, H. Doyle, S. Moynihan, A. Cuddihy, G. Redmond, *Appl. Phys. Lett.* **2005**, *86*, 201114.
[17] S. V. Kershaw, W. K. Yiu, A. Sergeev, A. L. Rogach, *Chem. Mater.* **2020**, *32*, 3930.
[18] Y. Prado, J. Qu, C. Gréboval, C. Dabard, P. Rastogi, A. Chu, A. Khalili, X. Z. Xu, C. Delerue, S. Ithurria, E. Lhuillier, *Chem. Mater.* **2021**, *33*, 2054.
[19] J. Qu, M. Weis, E. Izquierdo, S. G. Mizrahi, A. Chu, C. Dabard, C. Gréboval, E. Bossavit, Y. Prado, E. Péronne, S. Ithurria, G. Patriarche, M. G. Silly, G. Vincent, D. Boschetto, E. Lhuillier, *Nat. Photonics* **2022**, *16*, 38.
[20] X. Shen, J. C. Peterson, P. Guyot-Sionnest, *ACS Nano* **2022**, *16*, 7301.
[21] D. Yokoyama, *J. Mater. Chem.* **2011**, *21*, 19187.
[22] M. Chen, L. Shao, S. V. Kershaw, H. Yu, J. Wang, A. L. Rogach, N. Zhao, *ACS Nano* **2014**, *8*, 8208.
[23] B. Zhu, M. Chen, Q. Zhu, G. Zhou, N. M. Abdelazim, W. Zhou, S. V. Kershaw, A. L. Rogach, N. Zhao, H. K. Tsang, *Adv. Mater. Technol.* **2019**, *4*, 1900354.
[24] X. Tang, M. M. Ackerman, P. Guyot-Sionnest, *ACS Nano* **2018**, *12*, 7362.
[25] Y. Yifat, M. Ackerman, P. Guyot-Sionnest, *Appl. Phys. Lett.* **2017**, *110*, 041106.
[26] X. Tang, G. fu Wu, K. W. C. Lai, *J. Mater. Chem. C* **2017**, *5*, 362.
[27] A. Chu, C. Gréboval, N. Goubet, B. Martinez, C. Livache, J. Qu, P. Rastogi, F. A. Bresciani, Y. Prado, S. Suffit, S. Ithurria, G. Vincent, E. Lhuillier, *ACS Photonics* **2019**, *6*, 2553.
[28] T. H. Dang, C. Abadie, A. Khalili, C. Gréboval, H. Zhang, Y. Prado, X. Z. Xu, D. Gacemi, A. Descamps-Mandine, S. Ithurria, Y. Todorov, C. Sirtori, A. Vasanelli, E. Lhuillier, *Adv. Opt. Mater.* **2022**, *10*, 2200297.
[29] P. Rastogi, A. Chu, C. Gréboval, J. Qu, U. N. Noumbé, S.-S. Chee, M. Goyal, A. Khalili, X. Z. Xu, H. Cruguel, S. Ithurria, B. Gallas, J.-F. Dayen, L. Dudy, M. G. Silly, G. Patriarche, A. Degiron, G. Vincent, E. Lhuillier, *Nano Lett.* **2020**, *20*, 3999.
[30] T. H. Dang, A. Khalili, C. Abadie, C. Gréboval, M. Cavallo, H. Zhang, E. Bossavit, J. K. Utterback, E. Dandeu, Y. Prado, *ACS Photonics* **2022**, *9*, 2528.
[31] T. H. Dang, A. Vasanelli, Y. Todorov, C. Sirtori, Y. Prado, A. Chu, C. Gréboval, A. Khalili, H. Cruguel, C. Delerue, *Nano Lett.* **2021**, *21*, 6671.
[32] J. Guan, J.-E. Park, S. Deng, M. J. H. Tan, J. Hu, T. W. Odom, *Chem. Rev.* **2022**, *122*, 15177.
[33] J. Guan, L. K. Sagar, R. Li, D. Wang, G. Bappi, W. Wang, N. Watkins, M. R. Bourgeois, L. Levina, F. Fan, S. Hoogland, O. Voznyy, J. M. de Pina, R. D. Schaller, G. C. Schatz, E. H. Sargent, T. W. Odom, *ACS Nano* **2020**, *14*, 3426.

[34] D. Schanne, S. Suffit, P. Filloux, E. Lhuillier, A. Degiron, *Appl. Phys. Lett.* **2021**, *119*, 181105.
[35] R. Guo, S. Derom, A. I. Väkeväinen, R. J. A. van Dijk-Moes, P. Liljeroth, D. Vanmaekelbergh, P. Törmä, *Opt. Express* **2015**, *23*, 28206.
[36] A. Caillas, S. Suffit, P. Filloux, E. Lhuillier, A. Degiron, *Nano Lett.* **2022**, *22*, 2155.
[37] H. Wang, A. Aassime, X. Le Roux, N. J. Schilder, J.-J. Greffet, A. Degiron, *Phys. Rev. Appl.* **2018**, *10*, 034042.
[38] G. M. Akselrod, M. C. Weidman, Y. Li, C. Argyropoulos, W. A. Tisdale, M. H. Mikkelsen, *ACS Photonics* **2016**, *3*, 1741.
[39] A. A. Sergeev, D. V. Pavlov, A. A. Kuchmizhak, M. V. Lapine, W. K. Yiu, Y. Dong, N. Ke, S. Juodkazis, N. Zhao, S. V. Kershaw, *Light Sci. Appl.* **2020**, *9*, 16.
[40] A. A. Sergeev, K. A. Sergeeva, D. V. Pavlov, A. A. Kuchmizhak, *Bull. Russ. Acad. Sci. Phys.* **2022**, *86*, S196.
[41] P. Geiregat, A. J. Houtepen, L. K. Sagar, I. Infante, F. Zapata, V. Grigel, G. Allan, C. Delerue, D. Van Thourhout, Z. Hens, *Nat. Mater.* **2018**, *17*, 35.
[42] S. M. Tenney, V. Vilchez, M. L. Sonnleitner, C. Huang, H. C. Friedman, A. J. Shin, T. L. Atallah, A. P. Deshmukh, S. Ithurria, J. R. Caram, *J. Phys. Chem. Lett.* **2020**, *11*, 3473.
[43] A. V. Sokolova, I. D. Skurlov, A. A. Babaev, P. S. Perfenov, M. A. Miropoltsev, D. V. Danilov, M. A. Baranov, I. E. Kolesnikov, A. V. Koroleva, E. V. Zhizhin, A. P. Litvin, A. V. Fedorov, S. A. Cherevkov, *Nanomaterials* **2022**, *12*, 4198.
[44] S.-Y. Nien, N.-F. Chiu, Y.-H. Ho, J.-H. Lee, C.-W. Lin, K.-C. Wu, C.-K. Lee, J.-R. Lin, M.-K. Wei, T.-L. Chiu, *Appl. Phys. Lett.* **2009**, *94*, 103304.
[45] N. E. Hecker, R. A. Höpfel, N. Sawaki, T. Maier, G. Strasser, *Appl. Phys. Lett.* **1999**, *75*, 1577.
[46] A. Neogi, C.-W. Lee, H. O. Everitt, T. Kuroda, A. Tackeuchi, E. Yablonovitch, *Phys. Rev. B* **2002**, *66*, 153305.
[47] H. Rigneault, F. Lemarchand, A. Sentenac, *JOSA A* **2000**, *17*, 1048.
[48] R. R. Chance, A. Prock, R. Silbey, in *Adv. Chem. Phys.*, John Wiley & Sons, Ltd, **1978**, pp. 1–65.
[49] P. Rastogi, A. Chu, T. H. Dang, Y. Prado, C. Gréboval, J. Qu, C. Dabard, A. Khalili, E. Dandeu, B. Fix, *Adv. Opt. Mater.* **2021**, *9*, 2002066.
[50] P. Bharadwaj, B. Deutsch, L. Novotny, *Adv. Opt. Photonics* **2009**, *1*, 438.
[51] H. Wang, Y. Guo, H. Hao, H. Bian, H. Aubin, Y. Wei, H. Li, T. Liu, A. Degiron, H. Wang, *ACS Appl. Mater. Interfaces* **2021**, *13*, 56476.
[52] J.-J. Greffet, P. Bouchon, G. Brucoli, F. Marquier, *Phys. Rev. X* **2018**, *8*, 021008.
[53] A. Yang, Z. Li, M. P. Knudson, A. J. Hryn, W. Wang, K. Aydin, T. W. Odom, *ACS Nano* **2015**, *9*, 11582.